The Astrophysical Journal, 908:162 (13pp), 2021 February 20 https://doi.org/10.3847/1538-4357/abd856

Deciphering the 3D Orion Nebula. III. Structure on the NE Boundary of the Orion-S Embedded Molecular Cloud

C. R. O'Dell[1], N. P. Abel[2], and G. J. Ferland[3]
[1] Department of Physics and Astronomy, Vanderbilt University, Nashville, TN 37235-1807, USA
[2] MCGP Department, University of Cincinnati, Clermont College, Batavia, OH 45103, USA
[3] Department of Physics and Astronomy, University of Kentucky, Lexington, KY 40506, USA
Received 2020 November 24; revised 2020 December 22; accepted 2021 January 3; published 2021 February 22

Abstract

We have extended the work of Papers I and II of this series to determine at a higher spatial resolution the properties of the embedded Orion-S Molecular Cloud that lies within the ionized cavity of the Orion Nebula and of the thin ionized layer that lies between the Cloud and the observer. This was done using existing and new [N II] (658.3 nm) and [O III] (500.7 nm) spectra that map the central region of the Orion Nebula (the Huygens region). Although our observations show that the surface brightness of the ionized layer on the Orion-S Molecular Cloud and that of the nearer foreground ionized layer are linked, the process by which this is done is unclear. It is shown that the Cloud modifies the outer parts of the Huygens region in the direction of the extended hot X-ray gas.

Unified Astronomy Thesaurus concepts: H II regions (694)

1. Introduction

This is the third of a series of papers (O'Dell et al. 2020, henceforth Paper I; O'Dell et al. 2021, henceforth Paper II) addressing structures within the Huygens region of the Orion Nebula revealed by high-velocity-resolution spectroscopy. Using spatially large samples of spectra, we determined in Paper II that the region containing the Orion-S Cloud was characterized by widely changing strengths of velocity components in [O III] (500.7 nm), a phenomenon most striking near a subregion called the Crossing. In this paper, we investigate this subregion using higher-spatial-resolution groupings of spectra.

The Crossing and the Orion-S Cloud are especially important features as they lie in the direction of the X-ray-bright (Güdel et al. 2008) portions of the nebula that are enclosed by the recently discovered [C II] outer shell (Pabst et al. 2019, 2020). The Orion-S Cloud must interrupt the flow of stellar wind in that direction and also cast a radiation shadow. In Paper IV (C. R. O'Dell et al. 2020c, in preparation), we will explore the Herbig–Haro flow designated as HH 269 that arises from within the Orion-S Cloud.

This paper differs from Papers I and II in dealing with sequences of higher-spatial-resolution slit spectra of about 3.″6–4.″0 width and 8″–13″ length rather than averages of spectra over $10'' \times 10''$ samples. Although the slit spectra have lower total signal-to-noise ratios (S/Ns), they are not blurred in spatial or spectral resolution by fine-scale structure in the nebula. We shall see that the sequences of spectra reveal patterns only hinted at in the large-sample studies.

1.1. Background of This Study

A line-of-sight ray out of the Orion Molecular Cloud (OMC) toward the observer first passes through a photon-dominated region (PDR; Stacy et al. 1993; Goicoechea et al. 2015) and then the overlying main ionization layer (MIL) predominantly photoionized by θ^1 Ori C. The MIL is stratified into two zones of ionization, ordered by increasing distance from the H II actual ionization front and the distance to the photoionizing star θ^1 Ori C. The zone closest to the ionization front is composed of He^o+H^+ and emits the collisionally excited [N II] (658.3 nm) line used in this study. The farther zone is composed of He^++H^+ and emits the collisionally excited [O III] (500.7 nm) line used in this study. Material from the PDR is continuously lost as the MIL gas expands as photoevaporation flow into the lower-density regions farther out. The expanding gas is accelerated away from the ionization front, with the result that the [O III] photoevaporation flow velocity should be greater than that of [N II]. This photoevaporation flow has been well modeled by Henney et al. (2005) and is not affected by the global motions seen in layers of gas beyond θ^1 Ori C.

The region immediately around θ^1 Ori C is of lower density due to a stellar-wind-blown bubble whose outer boundary is shown in projection by a High Ionization Arc (O'Dell et al. 2020). Within the bubble is the Orion-S Molecular Cloud that is seen in absorption against the MIL radio continuum (Johnston et al. 1983; Mangum et al. 1993; van der Werf et al. 2013). The observer's side of the Orion-S Molecular Cloud is illuminated by θ^1 Ori C, producing an ionized layer that is the optically brightest portion of the Huygens region (Paper II). Proceeding outward, it encounters a layer of ionized gas designated as the nearer ionized layer (NIL; Abel et al. 2019), Papers I and II. Farther out still, there are two layers of atomic gas and H_2 (Abel et al. 2016). These were discovered in the H I 21 cm absorption (van der Werf & Goss 1989), and more recently, it was found that one of these layers is part of an expanding outer shell covering the entire extended Orion Nebula (Güdel et al. 2008) seen in [C II] 158 μm emission (Pabst et al. 2019, 2020).

In Papers I and II, we drew on the high-spectral-resolution Spectroscopic Atlas of Orion Spectra (García-Díaz et al. 2008, henceforth "the Atlas"), compiled from a series of north–south spectra at intervals of 2″. The Atlas has a velocity resolution of 10 km s^{-1} and a seeing-limited spatial resolution of about 2″. We analyzed high-S/N spectra of [N II] and [O III], averaged over spatial boxes of $10'' \times 10''$ and groupings of these samples into larger areas called groups and regions. In Paper I, we established the large-scale properties of the Huygens region (the well-studied bright region usually identified with M42, the

Orion Nebula), establishing that this region has a series of large-scale structures, the innermost being the optically bright main ionization front (MIF) and the outermost being a veil of atomic and molecular gas.

In Paper II, we explored at low spatial resolution the region to the SW of the dominant ionizing star θ^1 Ori C, establishing that the area including the Orion-S Cloud defies explanation by simple models. The low-ionization group was marked by very different behaviors of radial velocities. In [O III], these velocities group at two values, contrary to the expectations of photoevaporation from an ionization front and is in contrast with the simpler behavior in [N II].

In the current paper, we target the low-ionization group, which overlies the third star formation region in the Huygens region, at higher spatial resolution. It lies 50″ at 234° from θ^1 Ori C and must be associated with the Orion-S Cloud (it lies at the NE corner of the 21 cm H I contour of the Orion-S Cloud. The Orion-S Cloud is seen in radio absorption lines (hence it must lie in front of a source of radio continuum). The young stars lie on the east side of the Cloud and are the source of many collimated molecular and ionized outflows (jets). Shocks associated with these jets span the Huygens region. Extrapolation of the jets backward gives their origins with varying degrees of accuracy. Good presentations of the radio sources and jets are in Figure 1 of O'Dell et al. (2009) and Figures 15, 16, and 17 of O'Dell et al. (2008). A more recent study (O'Dell et al. 2015) refines the idea that although the sources are embedded and not seen in the optical, they lie close enough to the PDR that many of their jets break out and become optically visible features. This means that the geometry of the nebula is very different near this star formation region.

1.2. Nomenclature and Adopted Values

The list of terms and adopted values is presented in Paper II, but additional terms are necessary for this study and an amended list is given below.

1. Slit spectra are narrow rectangular areas of samples analogous to a short-slit spectrum.
2. Profiles are the data from a series of slit spectra ordered along a single direction.
3. Adjacent samples are a set of spectra selected to avoid the High Ionization Arc and the region surrounding the intersection of the profiles called the Crossing.
4. Samples are areas of 10″ × 10″ within which spectra from a spatially resolved atlas of spectra of certain emission lines have been averaged.
5. Regions are groupings of samples.
6. Sectors are groupings of adjacent samples, samples, and regions grouped by orientation relative to the Crossing.
7. The adopted distance is 388 ± 5 (Kounkel et al. 2017).
8. The adopted velocity for the background PDR is $V_{\rm PDR} = 27.3 \pm 0.3$ km s^{-1} (Goicoechea et al. 2015).
9. All velocities are expressed in km s^{-1} in the Heliocentric system (local standard of rest velocities are 18.1 km s^{-1} less).
10. Directions such as northeast and southwest are often expressed in short form as NE and SW.

1.3. Outline of This Paper

In Section 2, we describe the division of the components of the resolved line profiles (Section 2.1), how the rectilinear arrays of spatially resolved spectra from the Atlas were used to create series of spectra of a few arcseconds width at orientations useful for analyzing the Orion-S Cloud and groupings of the slit spectra into "adjacent samples" of higher S/N (Section 2.3). The location of the adjacent samples and their grouping are described in Section 2.3.1. Profiles previously presented (O'Dell 2018) are presented in Section 4, now annotated for the current study. The methods of analysis of the spectra are described in Section 3. An analysis of the profiles is presented in Section 4. A compilation of the data from Papers I and II, and this paper is given in Section 5. Section 6 discusses the observational properties and their relation to the 3D properties of the Orion-S Cloud and a summary of our conclusions and recommendations appear in Section 7. The Appendix presents a detailed study of an important small feature on the Orion-S Cloud.

2. Observations

2.1. Characteristic Velocity Systems

In Papers I and II, we have described how the spectra were created and deconvolved into velocity components. We repeat their description presented in descending velocity. $V_{\rm scat}$ (ascribed to backscattering from dust particles in the background PDR), $V_{\rm new}$ and $V_{\rm red,[O\,III]}$ (the former ascribed to material in the High Ionization Arc feature and the latter to material accelerated toward the host OMC by the stellar wind of θ^1 Ori C) or material that would normally be assigned to $V_{\rm long,[O\,III]}$ except for when the $V_{\rm short,[O\,III]}$ component is much stronger, $V_{\rm long,[O\,III]}$ (ascribed to emission from the ionized layer, the MIF, on the OMC, or the ionized layer of the Orion-S Cloud facing the observer, and $V_{\rm short,[O\,III]}$ (usually weak and ascribed to a foreground NIL lying in the foreground of θ^1 Ori C). These components are seen in both the [N II] and [O III] emission lines. In Paper I and earlier studies, the $V_{\rm short,[N\,II]}$ and $V_{\rm short,[O\,III]}$ components were called $V_{\rm low}$ and the $V_{\rm long}$ components were called $V_{\rm mif}$. As in Paper II, when discussed as emission from specific physical layers, the terms $V_{\rm mif}$ and $V_{\rm NIL}$ are used.

2.2. Twin Strong Components are Seen in Spectra within the Crossing

In Papers I and II, the strong MIF velocity component usually dominated each spectrum, although in Paper II, we found samples where $V_{\rm short}$ was stronger and $V_{\rm long}$ was not detected. Typical spectra and the shortcomings of deconvolution of the weaker secondary components were discussed and illustrated (O'Dell 2018; O'Dell et al. 2020). Such spectra were encountered in the present study, but in the regions within the Crossing, we often found that $V_{\rm short,[O\,III]}$ and $V_{\rm long,[O\,III]}$ components are both strong.

In Figure 1, we show a good example of a twin strong component [O III] spectrum. This is spectrum 29 in the south–

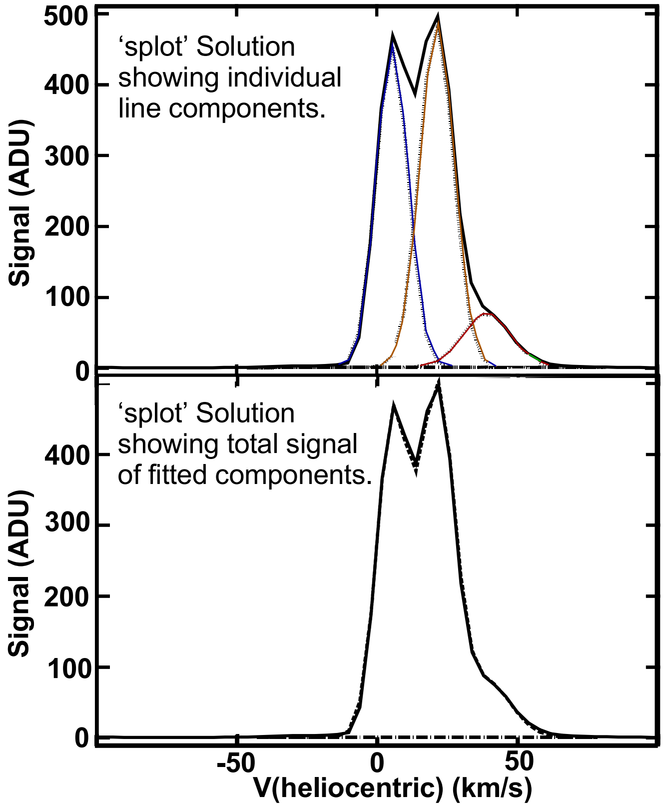

Figure 1. This spectrum illustrates [O III] spectra in the middle of the Crossing region, as described in Section 2.2. The top panel shows the observed line profile in black and the fitted components in color ($V_{\rm short}$—blue, $V_{\rm long}$—orange, $V_{\rm scat}$—red). In the lower panel, the observed line profile is in solid black, and the composite of the three fitted components is a barely distinguishable dotted line. The solutions using IRAF are $V_{\rm short,[O\,III]} = 5.3$ km s^{-1} ($S_{\rm short,[O\,III]}/S_{\rm long,[O\,III]} = 0.86$), $V_{\rm long,[O\,III]} = 21.0$ km s^{-1} ($S_{\rm long,[O\,III]} = 1.00$), and $V_{\rm scat,[O\,III]} = 39.1$ km s^{-1} ($S_{\rm scat,[O\,III]}/S_{\rm long,[O\,III]} = 0.23$).

north profile (Figure 5) and was deconvolved using the IRAF[4] task "splot."

2.3. Higher-spatial-resolution Slit Spectra

We use small spatial samples as we study the Crossing, whereas in Papers I and II we used $10'' \times 10''$ samples. This allowed an appropriately better spatial resolution in the Crossing. This was done using the same sequences of spectra as in O'Dell (2018) and newly created N–S sequences of spectra.

2.3.1. Previously Used Slit Spectra Profiles

The first type of sample is taken from O'Dell (2018), where a series of pseudo-slit spectra of approximately $3\overset{''}{.}8 \times 8''$–$13''$ were gathered into congruent sequences called profiles. Their locations are shown in Figure 2 and the profiles themselves in Figure 5. These are the same as in O'Dell (2018) except that they are now annotated for this study. Our analysis of these profiles is quite different than in O'Dell (2018) in that we now recognize the importance of the center of the Crossing and know when to group spectra into higher-S/N data.

4 IRAF is distributed by the National Optical Astronomy Observatories, which is operated by the Association of Universities for Research in Astronomy, Inc. under cooperative agreement with the National Science Foundation.

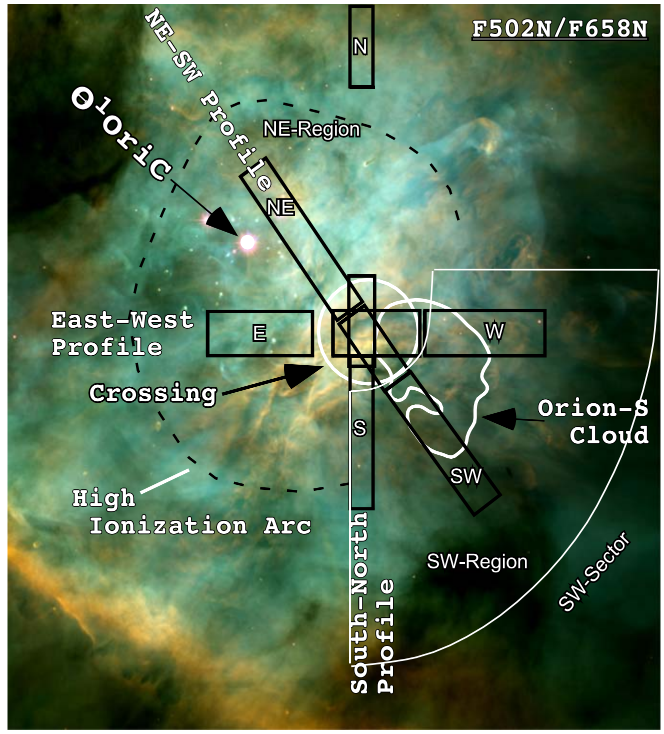

Figure 2. This $194'' \times 216''$ (0.36 × 0.40 pc) field of view (FOV) with north up and east to the left encloses the optically brightest part of the Huygens region. It is centered 45″ at P.A. (position angle) = 215° from θ^1 Ori C. The background image is from HST WFPC2 images coded by color (F658N, [N II] Red; F656N, Hα, Green; F502N, [O III], Blue) (O'Dell & Wong 1996). It shows the location of the adjacent and Crossing samples discussed in Section 2.3. The three Crossing samples for each profile are not named because of crowding but are shown. The Crossing circle has a diameter of 30″ and is centered at 5:35:13.95–5:23:49.2 (2000). The SW sector white lines show the boundaries for those samples to the SW that exclude Crossing samples.

Some groups are within the Crossing (called the Crossing samples) and others (called the adjacent samples) were selected to be close to the Crossing but avoided highly structured regions outside of the low-ionization group. The Crossing samples do not overlap completely, thus their results need not be exactly the same, but collectively they are representative of conditions within the Crossing.

Upon examination of the results for the profiles, we identified three regions of similar data. The NE sector includes the north, NE, and east adjacent samples; the Crossing contains the central adjacent samples; and the SW sector contains the south, SW, and west adjacent samples. Their locations are shown in Figure 2.

We present the averaged data of the multiple samples in Table 1. Reading left to right, one sees a progression of samples essentially flowing from the NE to the SW of the Crossing. Vertically, the results are ordered with the [N II] data in the first five lines, the [O III] data in the next five, and the joint [N II] and [O III] data on the last line.

2.3.2. Newly Created Slit Spectra Sequences

The second type of sample was created for this study. Within the Crossing, sequences of twelve $2\overset{''}{.}0$ spectra at intervals of $4''$ in right ascension (R.A.) were made, as shown in Figures 3 and 4. This rectilinear array has the advantage of higher spatial

Table 1
Data from the Profile Spectra Used in This Study[a]

	NE-sector Adjacents	Crossing	SW-sector Adjacents
$V_{\mathrm{long,[N\ II]}}$	19 ± 1	22 ± 1	19 ± 1
$V_{\mathrm{short,[N\ II]}}$	2.6 ± 2.0	4.6 ± 2.0	0.8 ± 2.4
$V_{\mathrm{scat,[N\ II]}}$	33 ± 2	38 ± 2	32 ± 1
$V_{\mathrm{scat,[N\ II]}} - V_{\mathrm{long,[N\ II]}}$	16 ± 3	16 ± 1	16 ± 1
$V_{\mathrm{long,[O\ III]}}$	16.2 ± 1.0	19 ± 2	17 ± 3[c]
$V_{\mathrm{short,[O\ III]}}$	4.9 ± 1.8	7 ± 2	6 ± 1
$V_{\mathrm{new,[O\ III]}}$	27 ± 2	…	…
$V_{\mathrm{red,[O\ III]}}$	…	19 ± 2	20 ± 3
$V_{\mathrm{scat,[O\ III]}}$	37 ± 3	39 ± 2	31 ± 2
$V_{\mathrm{scat,[O\ III]}} - V_{\mathrm{long,[O\ III]}}$	20.9 ± 3.7	20 ± 3	18 ± 3
$S_{\mathrm{long,[N\ II]}}/S_{\mathrm{long,[O\ III]}}$[b]	2.1 ± 0.9	5.7 ± 1.6	…
$S_{\mathrm{long,[N\ II]}}/S_{\mathrm{short,[O\ III]}}$	26.5 ± 18.1	5.4 ± 1.2	3.4 ± 1.8
$S_{\mathrm{long,[N\ II]}}/)$	…	…	…
$(S_{\mathrm{long,[O\ III]}} + S_{\mathrm{short,[O\ III]}})$	1.94 ± 0.67	2.9 ± 0.6	1.7 ± 0.3

Notes.
[a] All velocities are heliocentric velocities in km s^{-1}.
[b] $S_{\mathrm{long,[N\ II]}}/S_{\mathrm{long,[O\ III]}} = 1.00$ corresponds to a calibrated surface brightness (erg s^{-1}cm^{-2}sr^{-1}) ratio of 0.13.
[c] Without the highly scattered N–S profile (19.6 ± 9.2) south adjacent values.

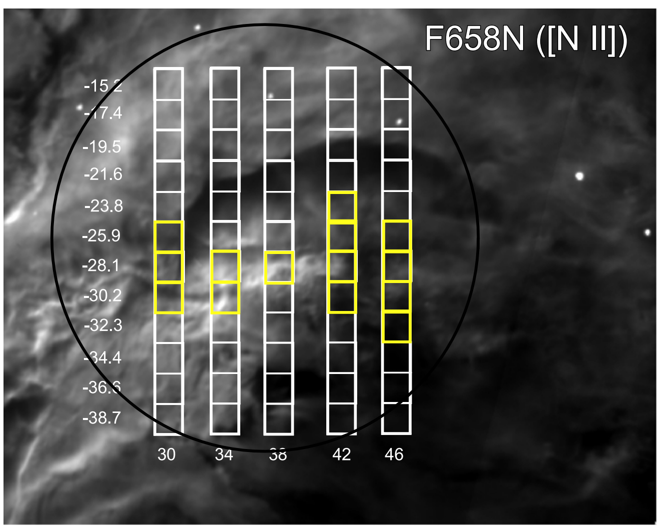

Figure 3. This $46'' \times 32''$ FOV is centered on the symmetry axis of the Dark Arc (within the Crossing which is shown with a dark circle). The boxes show the locations of the sampled spectra as discussed in Section 6. Those outlined in yellow define the Extended Ledge samples, those to the north (up) the Dark Arc-north samples, and those to the south the Dark Arc-south samples. The columns are marked with the west displacement in arcseconds from θ^1 Ori C, and the individual north–south spectra in arcseconds south of θ^1 Ori C. The image was made with the HST WFPC2 camera in the [N II] filter (F658N).

resolution ($2'' \times 2''$), and it better samples a nearly linear E–W feature in the middle of the Crossing. This is a well-defined "squiggly" feature, called here the Extended Ledge, that was discussed in O'Dell et al. (2015; where it was called the west jet). We determined membership in the Extended Ledge using higher surface brightnesses (SBs) and velocities as a guide and then derived averages of regions to the north and south of this (the Crossing-north and Crossing-south spectra groups, henceforth north array and south array), with the results shown in Tables 2–4. We believe that the disadvantage of averaging over varying features is appropriate because of the many samples in these groups.

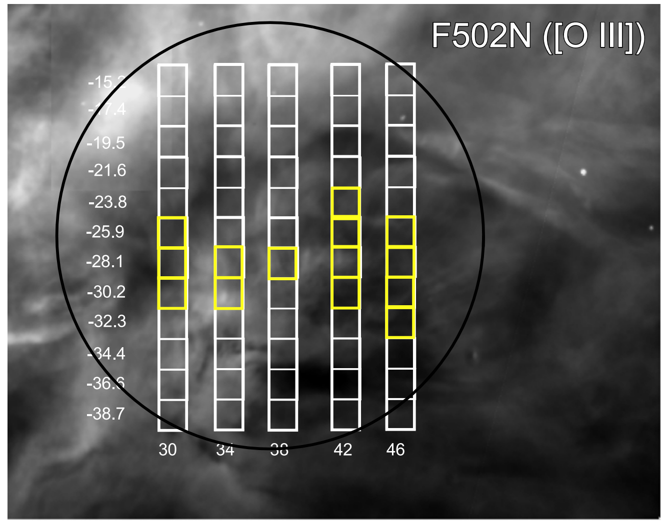

Figure 4. Like Figure 3 except now showing the [O III] F502N image.

Within the Extended Ledge, there is a [N II]-bright E–W linear feature. Because of its lack of apparent motion in the plane of the sky, this is not part of a moving jet. It is most likely to be a small portion of the MIF that is almost along the observer's line of sight. We now refer to this as the Ledge, and it must be a small local escarpment with the higher side to the south. There are other features that are strong in [O III] on both sides of the Ledge, with the ones on the west have measurable tangential motions. The Extended Ledge and its location are shown in Figures 3 and 4. The Ledge is pointed out in Figure 6.

The Ledge is discussed in detail in the Appendix.

In addition to velocity components that fit into the usual classifications, very blue and weak [O III] velocity components were seen in a few of the $34''$ west, $42''$ west, and $46''$ west profiles.

The data from these three regions are given within Tables 2–4. In addition, results from Papers I and II are given for regions outside these samples.

3. Analytic Tools

3.1. Velocity Variations when Crossing Tilted Ionization Layers

A velocity profile across an escarpment such as the Bright Bar will produce a single velocity peak, followed by a decrease to the velocity in the region beyond the escarpment, as shown in Figure 6 of O'Dell (2018). When a profile crosses a discreet cloud, one would expect to see a double velocity peak, the first on the side illuminated by θ^1 Ori C, the other on the far side of the cloud. The magnitude of the velocity variations depend on V_{PDR} and V_{evap} (the photoevaporation flow velocity). When the geometry is flat on, the observed V_{long} will be $V_{\mathrm{PDR}} - V_{\mathrm{evap}}$. As the MIF becomes tilted, the projection of the V_{evap} components will be reduced and at an edge-on geometry, one expects $V_{\mathrm{long}} = V_{\mathrm{PDR}}$. If the tilt is not completely edge on, the V_{long} variation will not be as great. As noted above, we would see this up and down velocity variation once in the profile of an escarpment and twice when the profile crosses both sides of an isolated cloud. The velocity pattern would be clearest when the profile cuts across the steepest part of the tilted front and would be less visible if the profile crosses it at an angle. Likewise, because of the difference in the thickness of their emitting

Table 2
Data from All [N II] Sources[a]

Group Name	$V_{\mathrm{long,[N\,II]}}$	$V_{\mathrm{short,[N\,II]}}$	$V_{\mathrm{scat,[N\,II]}} - V_{\mathrm{long,[N\,II]}}$	$S_{\mathrm{scat,[N\,II]}}/S_{\mathrm{long,[N\,II]}}$
NE Region	22 ± 2	6 ± 4	18 ± 4	0.06 ± 0.03
Inside Group	22 ± 3	3 ± 1	17 ± 2	0.07 ± 0.05
NE Sector	19 ± 1	3 ± 2	16 ± 3	0.11 ± 0.04
Low-ioniz. Group	21 ± 2	6 ± 3	16 ± 1	0.08 ± 0.03
North Array	22 ± 1	5 ± 2	16 ± 1	0.13 ± 0.05
Extended Ledge	25 ± 2	7 ± 2	17 ± 2	0.08 ± 0.05
South Array	24 ± 1	5 ± 2	19 ± 2	0.04 ± 0.02
SW Sector	19 ± 1	1 ± 2	16 ± 1	0.13 ± 0.03
Outside Group	19 ± 2	3 ± 3	16 ± 1	0.13 ± 0.04

Note.
[a] All velocities are heliocentric velocities in km s^{-1}.

layers, we would expect to see the pattern better in the thinner $V_{\mathrm{mif,[N\,II]}}$-emitting layer than the thicker $V_{\mathrm{mif,[O\,III]}}$-emitting layer.

The Bright Bar is the best example of a single-peaked velocity profile indicating that it is the edge of an escarpment and provides aid when looking at similar features. The ionized portion shows a signal peak and a velocity maximum that is expected (O'Dell 2018), and infrared and radio studies of neutral gas show the stratified presence of atoms and molecules consistent with and verifying PDR models (Tielens et al. 1993; Goicoechea et al. 2016).

The velocities and relative strengths of both the [N II] and [O III] lines are presented in Table 1.

3.2. Velocity Differences of the V$_{scat}$, V$_{long}$, and V$_{short}$ Components

As noted previously (Paper II), there is an expected relation between an emitting layer velocity (V_{emit}) and its backscattered component velocity (V_{scat}) and $V_{\mathrm{scat}} - V_{\mathrm{emit}}$ that is dependent upon the photoevaporation flow velocity (V_{evap}), V_{PDR}, and the tilt of the MIF. Under the assumption that the tilt is the same for the MIF and the V_{emit}-producing layer and that V_{evap} is constant throughout the area being examined, a flat-on view would have $V_{\mathrm{scat}} - V_{\mathrm{emit}} \simeq 2 \times V_{\mathrm{evap}}$ (Henney 1998). If the tilt increases toward an edge-on configuration, the line-of-sight component of V_{evap} will decrease, producing a decrease in the observed $V_{\mathrm{scat}} - V_{\mathrm{emit}}$ and an increase in the observed V_{emit}. The application of this information is discussed in Section 6.3.

3.3. Relative Strength of the Redshifted Backscattered Component

The ratio of signals (S) of the redshifted shoulder component of an observed line compared with a lower-velocity component informs the question of what emission-line component is being backscattered. The observed ratio $S_{\mathrm{scat}}/S_{\mathrm{comp}}$ must be much less than unity, reflecting the fact that the effective albedo must be low, unless there is a strong backscattering phase function. A large ratio means that this V_{comp} is not the source. If the source and the PDR are widely separated, the ratio will be unusually small.

3.4. Surface Brightness Variations

For a photoevaporating ionization front, the SB in a H I recombination line varies as the incident ionizing radiation (Baldwin et al. 1991; Osterbrock & Ferland 2006). For a face-on flat MIF, this means that there would be a monotonic decrease in the SB at increasing distances (in the plane of the sky) from the sub-θ^1 Ori C position. A concave MIF would have a slower decrease in SB with increasing angular distance and a convex MIF would have a more rapid decrease. The general concave structure of the inner Huygens region is well established. Features within the Huygens region, such as the Bright Bar, are explained as steep rises in the MIF. The high SB there is explained by both the ionizing flux increasing due to the tilt and the fact that one is looking at the emitting layer edge on.

More recently (O'Dell 2018), the same geometry has been applied to explain why the brightest part of the nebula occurs to the NE of the Orion-S Cloud. Although the increase in surface brightness is certainly due in part to the tilt, the proximity to θ^1 Ori C of the NE boundary to the Orion-S Cloud must also be very important. In Paper I, we established that the distance of θ^1 Ori C from the MIF ionization boundary was in the range 0.1–0.2 pc. The central value of 0.15 pc corresponds to 81″ if projected onto the plane of the sky. The peak surface brightness SB in [N II] occurs at 33″ (0.061 pc) from θ^1 Ori C in the plane of the sky. In Section 4.1, we pointed out that the Cloud is no closer to the observer than the plane including θ^1 Ori C or 0.05 pc (27″) beyond that plane. The corresponding range of physical distances between θ^1 Ori C and the NW edge of the Cloud is 0.061–0.079 pc—both are closer to θ^1 Ori C than the θ^1 Ori C to the MIF ionization boundary. Even without consideration of the enhancement due to looking along an emitting layer seen edge on, this explains why the SB in the Huygens region is highest there.

Of course, the expectations for the SB becomes more complex when dealing with [N II] and [O III] emission that occur in different zones within the ionized hydrogen layer, but even for their emission, the first-order expectations remain the same after considering that the [N II]-emitting layer is thinner and closer to the actual ionization front than the [O III]-emitting layer. However, if a region is lower ionization, then [N II] emission will be enhanced relative to the [O III] emission.

4. Analysis of the Profiles

4.1. Analysis of the Profiles in and near the Crossing

The northeast side of the Orion-S Cloud shows the velocity and ionization changes characteristic of an ionization front viewed edge on (Mesa-Delgado et al. 2011; O'Dell 2018; O'Dell et al. 2021), illuminated by θ^1 Ori C. The transition is shown in Figure 2, where the [O III]-dominated region

Table 3
Data from All [O III] Sources: Velocities[a]

Group Name	$V_{\text{long,[O III]}}$	$V_{\text{short,[O III]}}$	$S_{\text{short,[O III]}}/S_{\text{long,[O III]}}$	$V_{\text{scat,[O III]}} - V_{\text{long,[O III]}}$	$V_{\text{scat,[O III]}} - V_{\text{short,[O III]}}$
NE Region	18 ± 2	8 ± 2	0.10 ± 0.03	19 ± 4	…
Inside Group	16 ± 2	3 ± 1	0.05 ± 0.03	18 ± 4	…
NE Sector	16 ± 2	5 ± 2	0.04 ± 0.09	21 ± 4	…
Low-ioniz. Group[b]	*13 ± 2(6)*	*8 ± 2(8)*	…[c]	*21 ± 3(6)*	*29 ± 5(5)*
North Array	$21 \pm 2(7)$[d]	$6 \pm 1(7)$	$0.8 \pm 0.2(7)$	$19 \pm 1(7)$	$35 \pm 2(15)$
North Array	$16 \pm 1(11)$[d]	$4 \pm 1(8)$	$0.2 \pm 0.1(8)$	$23 \pm 2(8)$	…
Extended Ledge	20 ± 2	6 ± 2	1.0 ± 0.3	19 ± 2	$34 \pm 2(14)$
South Array	18 ± 2	7 ± 2	$3.2 \pm 1.0(7)$[d]	16 ± 1	$28 \pm 3(20)$
South Array			$0.9 \pm 0.2(9)$[d]	21 ± 1	…
SW Sector	$20 \pm 3(9)$	$8 \pm 2(9)$	$10.3 \pm 1.9(8)$[d]	$15 \pm 2(9)$	$27 \pm 4(9)$
SW Sector	$17 \pm 2(11)$	$5 \pm 2(11)$	$1.0 \pm 0.7(13)$[d]	$19 \pm 2(11)$	$31 \pm 2(11)$
Outside Group[b]	…	*11 ± 2*	$\gg 1$	…	*24 ± 2*

Notes.
[a] All velocities are heliocentric velocities in km s^{-1}.
[b] Results are affected by the unusually large FWHM of the $V_{\text{long,[O III]}}$ components.
[c] $V_{\text{long,[O III]}}$ and $V_{\text{short,[O III]}}$ were not found in the same samples.
[d] Samples group around these values.

transitions to a [N II]-dominated region along an SE–NW line. To the SW of this line lies the Orion-S Cloud ionized on the observer's side by θ^1 Ori C. Our Crossing samples are taken in the region of the Dark Arc feature (see Section 4.2.4) and overlap the NE 21 cm absorption boundary of the Orion-S Cloud (van der Werf et al. 2013). The Orion-S Cloud is also seen in absorption in H_2CO (Johnston et al. 1983; Mangum et al. 1993). The velocities of these features are the same as the OMC in this direction (Tatematsu et al. 1998; Peng et al. 2012; Troland et al. 2016). Because they are seen in absorption against an ionized gas continuum, the common interpretation is that this is a cloud lying within the main cavity of the nebula with portions of the MIF lying behind it. In Paper I, we established that the Cloud lies at the same distance from the observer as θ^1 Ori C or no more than 0.05 pc beyond it.

4.2. Velocity Variations

Given the guidelines described in Section 3.1, we can use the velocity variations in the profiles shown in Figure 5 to determine the geometry of the Crossing.

4.2.1. What do Velocity Variations in [N II] Tell Us?

Because the [N II] emission comes from a thin layer close to an ionization front, it is not surprising that the $V_{\text{long,[N II]}}$ changes demonstrate more continuous profiles than $V_{\text{long,[O III]}}$. In this section, we will discuss the $V_{\text{long,[N II]}}$ profiles and have always assigned the strongest component to $V_{\text{long,[N II]}}$.

It has been established (Mesa-Delgado et al. 2011; O'Dell 2018) that the Orion-S Crossing is immediately southwest of an ionization front viewed more nearly edge on, like the Bright Bar. The question then becomes whether its velocity profiles show a single peak (hence it is an escarpment) or a double peak (hence it is a cloud illuminated on both sides).

Each profile shows a slightly different variation in $V_{\text{long,[N II]}}$, reflecting the fact that they trace different paths across the Crossing and nearby areas. The E–W profile shows a broad peak in $V_{\text{long,[N II]}}$ occurring at spectrum 13 and a small local rise at spectrum 20, which lies on the east boundary of the Cloud's 21 cm absorption boundary. Proceeding north in the S–N profile shows two velocity peaks in $V_{\text{long,[N II]}}$, the first at spectrum 28 (closest to a surface brightness maximum) and a second at spectrum 21 (outside of the Crossing, but well inside of the southern crossing of the High Ionization Arc so that it is not the source of this velocity peak). Farther north, there is a pair of velocity peaks (spectra 42 and 48) as one crosses the High Ionization Arc, indicating that this is a shell of material. The NE–SW profile shows a peak in $V_{\text{long,[N II]}}$ near spectrum 10, with others at spectra 13 and 20. The peak at spectrum 13 may not be real as the surrounding spectra $V_{\text{long,[N II]}}$ lines are broad and may be blends of higher- and lower-velocity components. This would mean that there is a peak at spectrum 10, followed by a continuous reduction until the weak peak at spectrum 20.

Taken together, the $V_{\text{long,[N II]}}$ profiles indicate the crossing of a tilted ionization front near the center of the Crossing, followed by a flattening of the front, then crossing the outer boundary of this higher feature at about 30″ from the center of the Crossing.

It is surprising that crossing the edge of a raised feature (in the middle of the Crossing) occurs displaced from the transition region shown in Figure 2. It is as if this is a local structure superimposed on the broader low-ionization group.

We can safely conclude that the profiles are across a raised feature (closer to the observer) because we see the expected local maximum in the surface brightness ($S_{\text{long,[N II]}}$) at each of the first $V_{\text{long,[N II]}}$ peaks (crossing a depressed feature would produce $S_{\text{long,[N II]}}$ minima because of shadowing of θ^1 Ori C radiation).

The $V_{\text{short,[N II]}}$ behavior is harder to track because it is a usually a weak feature on the blue shoulder of the much stronger $V_{\text{long,[N II]}}$ component. The limitations of similar spectra are discussed quantitatively in O'Dell (2018) and Paper I. The lower S/N of the smaller spectra as compared with the $10'' \times 10''$ samples used in Papers I and II means that we cannot now use the V_{long} data except where its signal becomes strong. These are discussed in Section 6.1.

4.2.2. What do Velocity Variations in [O III] Tell Us?

Velocity variations in [O III] are much more complex than in [N II]. The $V_{\text{short,[O III]}}$ component is often strong and important, whereas in [N II] it was always weak as compared with

Table 4
Data from All [O III] Sources: Signal Ratios[a]

Group Name	$S_{\rm scat,[O\ III]}/S_{\rm long,[O\ III]}$	$S_{\rm scat,[O\ III]}/S_{\rm short,[O\ III]}$	$S_{\rm scat,[O\ III]}/S_{\rm both,[O\ III]}$[b]	$S_{\rm long,[N\ II]}/S_{\rm long,[O\ III]}$	$S_{\rm long,[N\ II]}/S_{\rm short,[O\ III]}$	$S_{\rm long,[N\ II]}/S_{\rm both,[O\ III]}$[b]
NE Region	0.06 ± 0.03	⋯	⋯	1.5 ± 0.5	⋯	⋯
Inside Group	0.07 ± 0.02	⋯	⋯	1.3 ± 0.1(15)	⋯	⋯
NE Sector	0.07 ± 0.03(31)	⋯	⋯	2.1 ± 0.9	⋯	⋯
Low-ioniz. Group[c]	*0.12 ± 0.04(6)*	*0.14 ± 0.07(7)*	⋯[d]	*2.8 ± 0.3(6)*	*3.1 ± 0.4(6)*	⋯[d]
North Array	0.16 ± 0.07(7)	0.19 ± 0.05(7)	0.10 ± 0.04(10)	4.6 ± 1.3(10)	5.6 ± 1.2(7)	2.5 ± 0.5(7)
North Array	0.14 ± 0.04(8)	0.7 ± 0.3(8)	0.10 ± 0.03(10)	2.5 ± 0.6(8)	13.3 ± 18.0(8)	2.1 ± 0.4(10)
Extended Ledge	0.26 ± 0.12	0.24 ± 0.08	0.13 ± 0.04	4.9 ± 1.2(10)[e]	5.0 ± 1.0(11)	3.0 ± 0.9
Extended Ledge				15.4 ± 5.4(3)[e]	0.88 ± 0.5(2)	
South Array	0.6 ± 0.3(7)	0.14 ± 0.05(6)	0.12 ± 0.03(6)	≫1	2.7 ± 0.5(6)	2.5 ± 0.6(6)
South Array	1.1 ± 0.3(10)	0.20 ± 0.08(10)	0.14 ± 0.05(9)	≫1	3.8 ± 1.1(10)	3.0 ± 0.9(10)
SW Sector	1.2 ± 0.6(11)	0.16 ± 0.10(9)	0.13 ± 0.06(9)	19.5 ± 8.8(9)	2.3 ± 0.4(9)	2.0 ± 0.3(9)
SW Sector	0.20 ± 0.06(9)	0.33 ± 0.11(11)	0.12 ± 0.03(11)	2.7 ± 0.7(10)	4.6 ± 1.6(11)	1.5 ± 0.1(11)
Outside Group[c]	⋯	*0.13 ± 0.04*	⋯	⋯	*1.6 ± 0.2*	⋯

Notes.
[a] All velocities are heliocentric velocities in km s^{-1}.
[b] $S_{\rm long,[N\ II]}/S_{\rm long,[O\ III]} = 1.00$ corresponds to a calibrated surface brightness (erg $s^{-1}cm^{-2}sr^{-1}$) ratio of 0.13.
[c] Results are affected by the unusually large FWHM of the $V_{\rm long,[O\ III]}$ components.
[d] $V_{\rm long,[O\ III]}$ and $V_{\rm short,[O\ III]}$ were not found in the same samples.
[e] Samples group around these values.

$V_{\rm long,[N\ II]}$. Examining the different $V_{\rm long,[O\ III]}$ profiles reveals the complex situation. The profiles in Figure 5 show components classified using the observed $V_{\rm r}$ as a guideline, with the redder assigned to $V_{\rm long}$ and the bluer to $V_{\rm short}$.

Proceeding from east to west in the E–W profile, we see that as one reaches the Crossing each spectrum suddenly has two significant components ($S_{\rm short,[O\ III]} \simeq S_{\rm long,[O\ III]}$) and they have two very different velocities. After passing through the Crossing $S_{\rm short,[O\ III]}$ becomes much less than $S_{\rm long,[O\ III]}$, but then increases and finally matches $S_{\rm long,[O\ III]}$, although the velocities of these two components remain about the same. $V_{\rm long,[O\ III]}$ has broad peaks at the same positions as $V_{\rm long,[N\ II]}$. The $V_{\rm short,[O\ III]}$ values are accurate (i.e., not questionable because of being a weak component on a stronger line's shoulder). This belief is reinforced by the fact that $V_{\rm short,[O\ III]}$ changes little as the components become of equal signal.

Proceeding south in the S–N profile, we again see two velocity peaks at spectra 42 and 48 as the shell of the High Ionization Arc is crossed. In this region, we see higher velocity components (labeled $V_{\rm new}$ in Figure 5 that are probably associated with the Arc. Moving further south the velocity of $V_{\rm long,[O\ III]}$ changes dramatically upon entering the Crossing. Suddenly the stronger component $V_{\rm long,[O\ III]}$ drops to velocity values usually assigned to $V_{\rm short,[O\ III]}$ and remains there for the remainder of the profile. They are redder (20 ± 3 km s^{-1}) and weaker components (labeled $V_{\rm red,[O\ III]}$ in Figure 5 that have a wide velocity dispersion and velocities similar to the $V_{\rm long,[N\ II]}$ components (22 ± 2 km s^{-1}) in the other adjacent samples in the SW sector (Table 1).

Proceeding SW in the NE–SW profile we first see little $V_{\rm long,[O\ III]}$ structure until reaching the Crossing, at which point the $V_{\rm long,[O\ III]}$ and $V_{\rm short,[O\ III]}$ components become comparable signals. Results from spectra 12–18 are ambiguous because the strongest line is broad and the lower $V_{\rm long,[O\ III]}$ values there are in between the previous $V_{\rm long,[O\ III]}$ and $V_{\rm short,[O\ III]}$ values. The few narrow lines at spectra 20–22 fall at velocities usually associated with the $V_{\rm long,[O\ III]}$ and $V_{\rm short,[O\ III]}$ systems.

4.2.3. What do the Velocity Differences Tell us About the Crossing Geometry?

Examination of $V_{\rm scat} - V_{\rm long}$ in Table 1 indicates that for the backscattered [N II] component, the well-defined difference of 16 km s^{-1} is close to the expected value of 14 ± 2 km s^{-1} for a flat-on viewing angle.

The difference for [O III] may change slightly, as the line of sight moves from the NE-sector adjacent samples (21 ± 4 km s^{-1}), through the Crossing (20 ± 3 km s^{-1}), to the SW-sector adjacent samples (18 ± 3 km s^{-1}). All of these are unimportantly lower than the predicted range 20 ± 6 km s^{-1}.

The agreements of observed and expected velocity differences indicate that the MIF emission is in fact being backscattered by the nearby underlying PDR. The smaller dispersion of the [N II] values indicates that there is not a big change in the viewing angle in the three regions. This is consistent with our intentionally not including the region of known high tilt on the NE boundary of the Orion-S Cloud. The same can be said for the [O III] emission, although with less certainty because of the larger probable errors.

4.2.4. Observed Surface Brightness Variations

The geometry of the nebula that produced the velocity variations described in Sections 4.2.1 and 4.2.2 should also produce variations in the apparent surface brightness (SB) of the nebula. In this section, we examine the SB variations using the signal in the Atlas as in O'Dell (2018), where the conversion to power units is also explained.

None of the profiles cross through θ^1 Ori C, but their minimum distances (the θ^1 Ori C-tangent) from that star should be marked by a local peak in SB. These θ^1 Ori C-tangent points (spectrum 36 for the S−N profile, spectrum −1 for the NE −SW profile, spectrum 3 for the E−W profile) are shown in Figure 5. In the absence of structure in the region covered by the profiles, we would expect to see a single peak in the SB at the θ^1 Ori C-tangent location with a monotonic drop in the SB in both directions away from this point. We see peaks in both

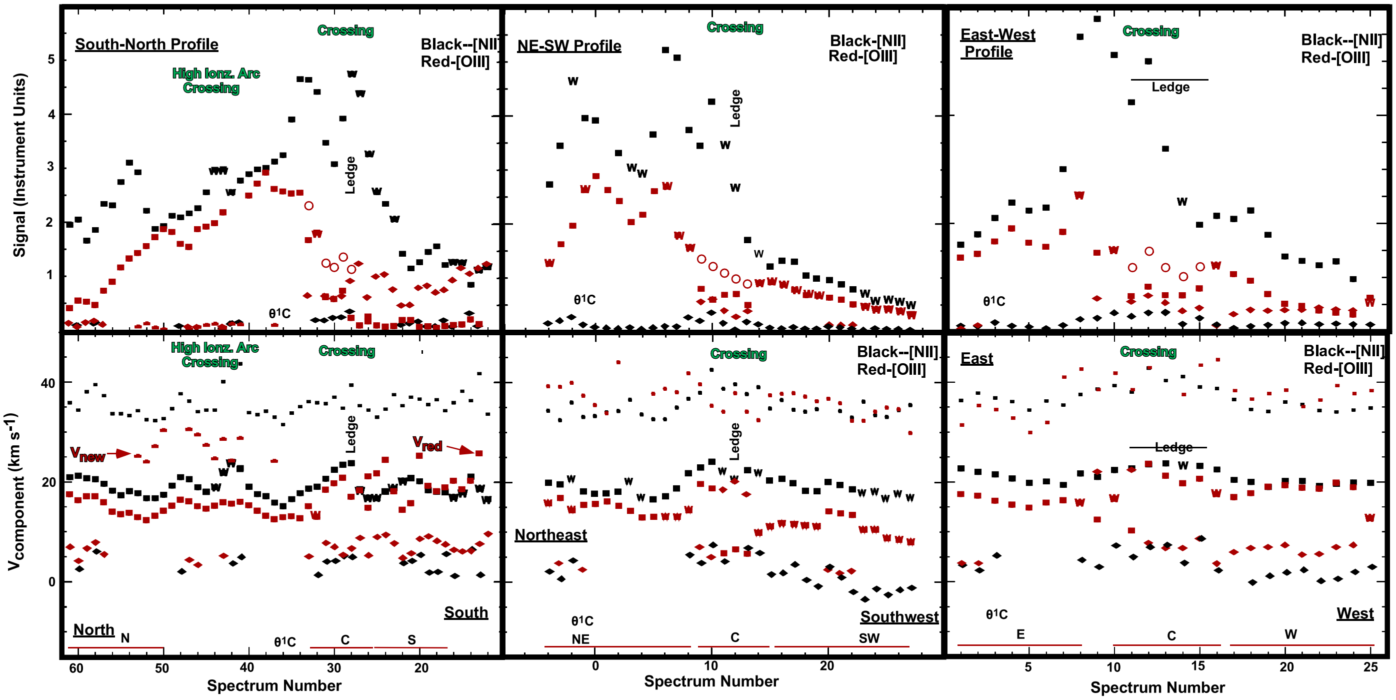

Figure 5. Like Figures 10–12 from O'Dell (2018) except annotated for this study. Large filled boxes: long components, small filled boxes: scattered components, horizontal boxes: $V_{\rm new}$ and $V_{\rm red,[O\,III]}$, and large filled diamonds: short components. Black indicates [N II] and red [O III]. The spectra spacing is 3$''$.6 for the S–N and NE–SW profiles, and 4$''$.0 for the E–W profile. θ^1 Ori C indicates the spectrum lying closest to θ^1 Ori C. The Orion-S Crossing indicates spectra within the Crossing. The low red lines indicate the spectra included in the adjacent samples. The letter W indicates where the FWHM of $V_{\rm long,[N\,II]} \geqslant 18.0$ km s^{-1} or when the FWHM of $V_{\rm long,[O\,III]} \geqslant 16.0$ km s^{-1}. The open red circles depict the sum of the $S_{\rm short,[O\,III]}$ and $S_{\rm long,[O\,III]}$ components in the Crossing.

ions near each of the θ^1 Ori C-tangent points and a continuous drop into the NE sector, interrupted only in the S−N profile where it crosses the High Ionization Arc and an even more removed feature to the north, seen only in $S_{\rm long,[O\,III]}$. Variations in $V_{\rm long,[N\,II]}$ and $V_{\rm long,[O\,III]}$ accompany the High Ionization Arc passage.

We also see variations in the SB in both ions as one traces outward (into the SW sector) from the θ^1 Ori C-tangent point. If these profiles simply traced across an escarpment, one would expect to see a monotonic rise to an SB maximum as the observed $V_{\rm long}$ increases. This should be more obvious in [N II] because its emitting layer is thinner. The passage of the escarpment accounts for the $S_{\rm long,[N\,II]}$ peaks at the S−N profile (spectrum 34), NE−SW profile (spectrum 7), and E−W profile (spectrum 9). Small increases in $V_{\rm long,[N\,II]}$ can be attributed to the passage across the escarpment.

It should also be noted that unlike [N II], the sum of the $S_{\rm long,[O\,III]}$ and $S_{\rm low,[O\,III]}$ components in the Crossing approximate the total $S_{\rm long,[O\,III]}$ value needed to provide a smooth interpolation of the SB over the Crossing as indicated by the open red circles in Figure 5. This is consistent with the dark features being less conspicuous in [O III]. The comparable strength of both components makes their measurements more accurate than when $S_{\rm low,[O\,III]}/S_{\rm long,[O\,III]}$ is low. The fact that the low components are strong raises the possibility that in the Crossing, the $V_{\rm short,[O\,III]}$-emitting layer is competing with the $V_{\rm long,[O\,III]}$-emitting layer for the higher-ionization-energy photons necessary to produce [O III] as discussed in detail in Paper II.

The feature called the Extended Ledge here appears to be a small escarpment region, with the south side being higher. It is denoted in Figure 6. Although it looks like a jet, there are no tangential velocities (O'Dell et al. 2015) on its east end but

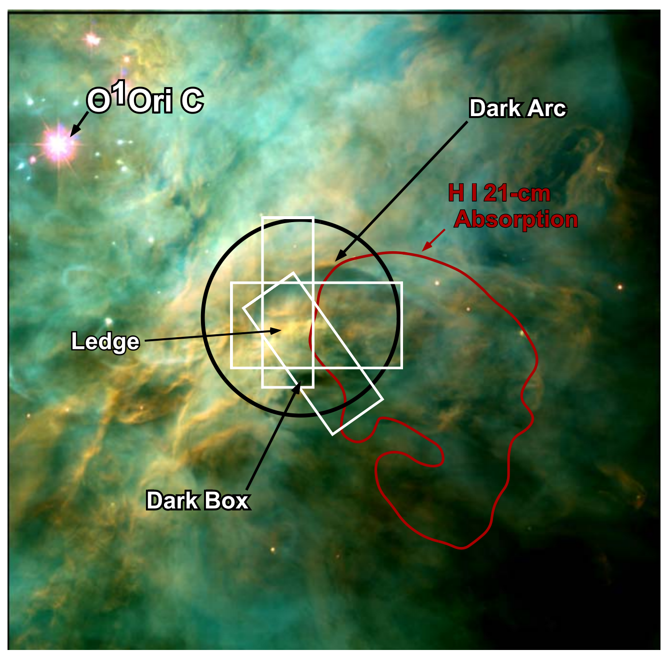

Figure 6. This 100$''$ × 98$''$ (0.19 × 0.18 pc) FOV is centered on the Crossing (black circle) region and encloses the optically brightest part of the Huygens region. The two small low-surface-brightness features (Dark Arc and Dark Box) discussed in Section 4.2.4 are labeled. The background image is from HST WFPC2 images coded by color (F658N, [N II] red; F656N, Hα, green; F502N, [O III], blue; (O'Dell & Wong 1996). The outer H I absorption contours with heavy red lines are from van der Werf et al. (2013). The white rectangles indicate the location of the Central sections of the three profiles.

several in [O III] and a few in [N II] beginning at its west end. It is studied in depth in Paper IV.

The point of passage across this east–west oriented feature (Figure 6) is marked by the word Ledge in each panel of Figure 5. It is drawn with a line in the E–W profile because the profile passes along the axis of the feature. At each marked position, there is an associated local peak in $S_{\mathrm{long,[N\,II]}}$, attributable to the feature. Similarly, there is an increase in $V_{\mathrm{long,[N\,II]}}$ at these locations. This important feature is discussed further in the Appendix.

It is probable that a feature known as the Dark Arc (O'Dell & Yusef-Zadeh 2000; O'Dell et al. 2015) also plays a role in the SB profiles. In Figure 6, we present our best-resolution color image. The Dark Arc and Dark Box low SB features are seen in both ions, especially [N II]. They are discussed in detail in Section 3.2.1 of O'Dell et al. (2015). Although they are not understood, they are thought to be regions of low emissivity near the ionized layer on the observer's side of the Cloud, possibly small scale escarpments produced by one or more of the many stellar outflows in this region. In the S–N and NE–SW profiles, the Dark Arc feature occurs at the SB minimum. In the E–W profile, the dip occurs at the spectrum including the east boundary of the Dark Arc, where it is nearly aligned N–S.

Examination of the [O III] profiles shows that the clear division into $V_{\mathrm{short,[O\,III]}}$ and $V_{\mathrm{long,[O\,III]}}$ components begins in the same samples that dip in [N II] SB. The $V_{\mathrm{long,[O\,III]}}$ SB drops to lower than interpolation from adjacent spectra, and the new $V_{\mathrm{short,[O\,III]}}$ spectra are of comparable strength to the $V_{\mathrm{long,[O\,III]}}$ components.

Most significant is that the total strength of the $V_{\mathrm{long,[O\,III]}}$ and $V_{\mathrm{short,[O\,III]}}$ components fall onto a smooth interpolation of adjacent values.

5. A Compilation of Data for the Large-scale Features and Groups

Averaged results for the samples described above and nearby regions from Papers I and II are given in Tables 2–4 In addition to the results of this study. The arrangement (top to bottom rows) is basically from NE to SW.

We have not used the results from the SW region discussed in Paper I because it overlaps with the multiple smaller groups identified here and in Paper II. Two groups rendered in italics are affected by the slightly larger FWHM of the $V_{\mathrm{long,[O\,III]}}$ component. In those (the low-ionization group and the outside group), this width means that there is no chance of seeing a weak companion component and their values must be used cautiously.

Where there are two lines of entries for a group in [O III], the property that showed the biggest division in entries is marked is marked [d] in Table 3 and [e] in Table 4. The composition of those subgroups was used to derive the other characteristics. When there was no obvious difference between the two groups, a single value is given. The line containing the higher $V_{\mathrm{long,[O\,III]}}$ subgroup is always located higher in Tables 3 and 4.

6. Discussion

The three compiled tables of data can be used to investigate the structure and properties of a NE–SW swath across the Huygens region.

Examination of the results in Tables 2–4 illustrates how the unusual behavior of the [O III] velocity components found over a large area in Paper II are first encountered in the Crossing, and that within the Crossing, the behavior originates near a narrow east–west feature, the Extended Ledge. To the NE, the $V_{\mathrm{short,[O\,III]}}$ component is weak compared with $V_{\mathrm{long,[O\,III]}}$, but this is reversed as one passes the Crossing.

These results refine the discovery in Paper II that the $V_{\mathrm{short,[O\,III]}}$ component appeared in five of the nine large samples that included all or part of the Crossing. In addition, the $V_{\mathrm{short,[O\,III]}}$ component appeared without a $V_{\mathrm{long,[O\,III]}}$ component in 15 other samples to the south and southwest of the Crossing. This indicates that although the two velocity systems may originate in the Crossing, they occur throughout the low-ionization group.

In contrast, the $V_{\mathrm{short,[N\,II]}}$ component is always weak compared with $V_{\mathrm{long,[N\,II]}}$. In Table 5, we see that $S_{\mathrm{short,[N\,II]}}/S_{\mathrm{long,[N\,II]}}$ is 0.14, 0.25, and 0.11 in the three supergroups.

We see in these tables that the [O III] properties within samples often break down into groupings (subgroups), reflecting the fact that within the scale of the features, there are a variety (at least two) of characteristics. The subgrouping begins in the north array and extends into the SW sector.

The data in Tables 2–4 can also be used to derive other properties of the regions sampled, as shown in the following subsections.

6.1. Supergroups and the Relation of the Short Velocity Features to the NIL

The NIL lies across much of the Huygens region and is best characterized in Paper I, where its velocity and relative strength are discussed and modeled, using data from near θ^1 Ori C. It is appropriate to see if the V_{short} components we examine in this study are part of the NIL or have been altered by the conditions on the ionized layer atop the Orion-S Cloud. We have done this using the velocities and signals.

We gathered the groups into "supergroups": the NE supergroup (NE region, inside group, NE sector), Crossing supergroup (north array, Extended Ledge, south array), and SW supergroup (SW sector). Within each supergroup, we created a subgroup where velocities and signals existed for all components. Within these subgroups, we determined the average $V_{\mathrm{short,[N\,II]}}$ and $V_{\mathrm{short,[O\,III]}}$, with the results shown in Table 5.

We also created average signals for the subgroups in both the long and short components of both ions. These are preceded by "Ave" in Table 5 and are more accurate measures of the SB, whereas signals over samples are a mix of features from different parts of the samples. The ± symbols do not indicate uncertainties; rather, they are the 1σ spreads of the samples. The average values are used in our discussion of ionization changes (Section 6.2).

$V_{\mathrm{short,[N\,II]}}$ shows the widest variation in value between the supergroups. The Crossing supergroup's value of 6 ± 3 is slightly higher than the interpolation (2.5 ± 2) between the adjacent supergroups. If this marginal evidence is accepted, then it is an indication that the [N II]-emitting layer of the NIL that lies in front of the Orion-S Cloud has been affected. However, the more positive value of the velocity difference is the opposite of what is expected from the interaction of gas flowing towards the observer from the Orion-S Cloud. In our discussion of the full profiles passing over the Crossing (Section 4.2.1), we saw that this region's $V_{\mathrm{long,[O\,III]}}$ values indicate that it is a raised region, which is consistent with its

Table 5
Data for Supergroups[a]

Property	NE Supergroup	Crossing Supergroup	SW Supergroup
$V_{\rm long,[N\,II]}$	21 ± 1	24 ± 1	19 ± 1
$V_{\rm short,[N\,II]}$	3 ± 2	6 ± 3	2 ± 2
$V_{\rm long,[O\,III]}$	19 ± 3	21 ± 2	18 ± 3
$V_{\rm short,[O\,III]}$	4 ± 2	6 ± 2	6 ± 2
Ave $S_{\rm long,[N\,II]}$	171.3 ± 90	412.5 ± 157	129 ± 27
Ave $S_{\rm short,[N\,II]}$	13.8 ± 4.4	37.5 ± 19	13.8 ± 3.8
Ave $S_{\rm long,[O\,III]}$	108.3 ± 47	71.4 ± 15	30.2 ± 20.2
Ave $S_{\rm short,[O\,III]}$	8.98 ± 5.3	62.1 ± 9	49.8 ± 23.2
Ave $S_{\rm long,[N\,II]}$/Ave $S_{\rm long,[O\,III]}$	1.6[b]	5.8	4.3
Ave $S_{\rm long,[N\,II]}$/Ave $S_{\rm short,[O\,III]}$	19.1[b]	6.6	2.6

Notes.
[a] All velocities are heliocentric velocities in km s^{-1}.
[b] Samples group around these values. Parentheses enclose the number of samples within each subgroup.

Table 6
Predicted and Observed Backscattering Velocities[a]

Velocity Component	Predicted ($V_{\rm scat} - V_{\rm comp}$)	Observed ($V_{\rm scat} - V_{\rm comp}$)	$S_{\rm scat}/S_{\rm comp}$
NE Sector			
$V_{\rm long,[N\,II]}$	16 ± 2	16 ± 3	0.11 ± 0.04
$V_{\rm long,[O\,III]}$	22 ± 4	21 ± 4	0.07 ± 0.03
$V_{\rm short,[O\,III]}$	44 ± 4	…[b]	…[c]
Crossing			
$V_{\rm long,[N\,II]}$	10 ± 2	16 ± 5	0.08 ± 0.05
$V_{\rm long,[O\,III]}$	17 ± 4	$21 \pm 2(25)$, $18 \pm 3(16)$[c]	$0.20 \pm 0.09(29)$, $1.0 \pm 0.3(15)$[c]
$V_{\rm short,[O\,III]}$	43 ± 3	$34 \pm 3(29)$, $29 \pm 3(15)$[c]	$0.30 \pm 0.17(27)$, $0.19 \pm 0.09(12)$[c]
SW Sector			
$V_{\rm long,[N\,II]}$	16 ± 2	16 ± 1	0.13 ± 0.03
$V_{\rm long,[O\,III]}$	17 ± 5	19 ± 2, $15 \pm 2(9)$	$0.20 \pm 0.09(11)$, $1.2 \pm 0.6(9)$
$V_{\rm short,[O\,III]}$	44 ± 4	$31 \pm 2(11)$, $27 \pm 4(9)$	$0.33 \pm 0.11(11)$, $0.16 \pm 0.10(9)$

Notes.
[a] All velocities are heliocentric velocities in km s^{-1}.
[b] No $V_{\rm short,[O\,III]}$ component is seen.
[c] Samples group around these values. Parentheses enclose the number of samples within each subgroup.

being part of the ionized layer on the observer's side of the Orion-S Cloud. If the higher value of $V_{\rm short,[N\,II]}$ is accepted, it could be due to interactions with the Orion-S Cloud's surface, thus arguing for a small separation of positions. In this case, the more positive velocity would have to arise from flow away from the NIL and the observer.

We see that $V_{\rm short,[O\,III]}$ is essentially constant across the supergroups at 5 ± 2 km s^{-1}. This places it at a characteristic velocity of the NIL and argues that the velocity of the [O III] component of the NIL is not affected by the Orion-S Cloud.

6.2. Changes of Ionization in and near the Crossing

Because we see remarkable changes in the $S_{\rm short,[O\,III]}/S_{\rm long,[O\,III]}$ ratio as one moves from the NE to the SW, it is important to determine if these are due to one component increasing while the other decreases, or vice versa. This is best done with the Ave signals given in Table 5.

There, we see that Ave $S_{\rm long,[N\,II]}$ has decreased more than a factor of 0.75 going from the NE to the SW side of the crossing, while Ave $S_{\rm long,[O\,III]}$ has dropped by a factor of 0.28. This means that the ratio of Ave $S_{\rm long,[N\,II]}$/Ave $S_{\rm long,[O\,III]}$ has changed from 1.6 to 4.3, as shown in Table 5. This supports the conclusion that the ionization drops with increasing distance from θ^1 Ori C. Much of this change of ratio is due to the dramatic drop in Ave $S_{\rm long,[O\,III]}$ SW of the Crossing while Ave $S_{\rm short,[O\,III]}$ has increased fivefold from the NE-supergroup values.

6.3. What Do We Learn from the Backscattering?

We can apply the methods described in Sections 3.1 and 3.3 to the interpretation of the regions immediately to the NE of the Crossing (the NE sector), the Crossing itself, and the regions immediately to the SW (the SW sector). For this, we have employed the spectra in the profiles, as described in Section 4. The results of our observations and predictions are shown in Table 6.

As noted in Section 3.3, the ratio $S_{\rm scat}/S_{\rm comp}$ should be much less than unity, and this can be used to verify that one has correctly identified the source of the $V_{\rm scat}$ component. This condition is satisfied for all of the [N II] samples and for most of the [O III] samples. However, in the Crossing, we see that the more numerous $V_{\rm long,[O\,III]}$ component satisfies the condition while in $V_{\rm short,[O\,III]}$ the less numerous ones do. The same pattern applies in the SW sector (although the population of the groups is about equal).

It is informative to compare the observed velocity difference ($V_{\rm scat} - V_{\rm comp}$) with the predicted value. For a flat-on region, the observed $V_{\rm comp}$ will be $V_{\rm PDR} - V_{\rm expansion}$ from which the photoionization flow velocity for each emission line can be calculated. We have used $V_{\rm PDR} = 27\ {\rm km\ s^{-1}}$ and from this calculated a predicted $V_{\rm scat} - V_{\rm comp}$. This value should decrease in a more highly tilted region.

In [N II], the long component is dominant (see Table 2). The agreement of the observed and predicted $V_{\rm scat,[N\ II]} - V_{\rm long,[N\ II]}$ values is good for the NE and SW sectors, which are not highly tilted, and the difference in the Crossing indicates the complexity of the region. The $S_{\rm scat,[N\ II]}/S_{\rm long,[N\ II]}$ values are always low enough to confirm that $V_{\rm long,[N\ II]}$ is the source of the backscattered light.

In the NE sector, $S_{\rm short,[O\ III]}/S_{\rm long,[O\ III]}$ is small (to the point that $V_{\rm short,[O\ III]}$ is not detected). The observed and predicted $V_{\rm scat,[O\ III]} - V_{\rm long,[O\ III]}$ are in good agreement.

In the Crossing, we see that the observed and predicted velocity difference is very different for [N II]. This probably reflects the complexity of this region owing to the many smaller regions with large tilts.

Also in the Crossing, we see that a larger sample satisfies the $S_{\rm scat,[O\ III]} - S_{\rm long,[O\ III]}$ requirement, but that its observed velocity different agree's less well than the smaller group. However, the probable errors are such that it may be indistinguishable. Neither $V_{\rm short,[O\ III]}$ group agrees with the predictions. Again, this indicates the complexity of the Crossing.

In the SW sector, the observed and predicted velocity differences for [N II] are excellent. Again, the $V_{\rm long,[O\ III]}$ component breaks down into favored and unlikely scatters, but both components agree equally well with the predictions. Like the Crossing, the observed and predicted values are highly discrepant.

In summary, we see that in [N II] the observed and predicted velocity differences are good in the NE and SW sectors, but poor in the complex Crossing. In [O III], we see that the agreement is good in the NE and SW sectors, but in the Crossing there are no good agreements.

6.4. A Different V$_{evap}$ Velocity for [O III]

The predicted values of $V_{\rm scat} - V_{\rm comp}$ in the previous section were calculated from inferred values of $V_{\rm evap}$, and that the velocity separation would be twice $V_{\rm evap}$. The argument can be reversed to use the observed velocity difference to derive $V_{\rm evap}$. This tells us that $V_{\rm evap,[N\ II]}$ is the same in all three supergroups, about $8 \pm 1\ {\rm km\ s^{-1}}$. Using the lower $S_{\rm scat,[O\ III]}/S_{\rm long,[O\ III]}$ groups give $V_{\rm evap,[O\ III]} = 10 \pm 1\ {\rm km\ s^{-1}}$. The slightly larger value for [O III] is consistent with the idea (Henney et al. 2005) that the [O III]-emitting zone is farther from the MIF and thus has been subjected to more acceleration.

7. Conclusions

1. The [N II] emission arises from a narrow layer along an ionization front. The $V_{\rm long,[N\ II]}$ component is always much brighter than the $V_{\rm short,[N\ II]}$ component. In the region nearest θ^1 Ori C, it clearly lies along the MIF and in the Crossing along the ionized surface of the Orion-S Cloud that faces the observer. To the SW, its location is uncertain as it could be either over the main body of the Orion-S Cloud or on the MIF of the nebula beyond the embedded Orion-S Cloud. Strong backscattering of its radiation indicates that it is always close to a dusty PDR.
2. The $V_{\rm short,[N\ II]}$ component arises from the NIL, the layer of gas lying on the observer's side of θ^1 Ori C and the Orion-S Cloud. Its surface brightness is the same in the NE supergroup and the SW supergroup, even though the latter is much more distant in the plane of the sky. The surface brightness is unexpectedly much higher in the Crossing supergroup. Its velocity is almost the same when sweeping from NE to SW, but there is a possible increase over the Crossing supergroup. If real, this would indicate that the NIL is closer to θ^1 Ori C than we calculated in Paper I.
3. The $V_{\rm long,[O\ III]}$ component arises from a thicker, more highly ionized region than $V_{\rm long,[N\ II]}$. Its velocity is almost constant when passing through the supergroups. Like $V_{\rm long,[N\ II]}$, the NE-supergroup emission arises from the MIF beyond θ^1 Ori C and the Crossing supergroup on the observer's side of the Orion-S Cloud. Again, the physical location is uncertain in the SW supergroup. Its SB decreases monotonically with increasing distance from θ^1 Ori C. The lack of an increase in the Crossing supergroup indicates that its emitting layer is thicker than the physical high point indicated by the [N II] profiles. The [O III] profiles indicate that at the Crossing, the SB begins to drop, and beyond the Crossing, $V_{\rm short,[O\ III]}$ is dominant. Within the Crossing, we see wide variations in $S_{\rm short,[O\ III]}/S_{\rm long,[O\ III]}$ and note that the SB variations suggest that the EUV radiation is being split between the $S_{\rm short,[O\ III]}$- and $S_{\rm long,[O\ III]}$-emitting regions.
4. $V_{\rm short,[O\ III]}$ is essentially constant across the NE–SW sweep. Taken alone, this would indicate that it always arises from the NIL. However, the SB of $V_{\rm short,[O\ III]}$ leaps in the Crossing supergroup and remains high into the SW supergroup. This behavior remains unexplained.
5. Within the peak of the rise upon which the Crossing is centered, there is a highly tilted low-ionization region facing the north.
6. The Orion-S Cloud produces changes to its SW, which is the direction of the hot gas giving rise to X-ray emission. However, there is no obvious link to the Outer Shell that covers the near side of the extended Orion Nebula.
7. There is a pressing need to refine the NIL modeling approach that we presented in Paper I and to apply it to various positions along the NE-SW sweep.

The observational data were obtained from observations with the NASA/ESA Hubble Space Telescope, obtained at the Space Telescope Science Institute (GO 12543), which is operated by the Association of Universities for Research in Astronomy, Inc., under NASA contract No. NAS 5-26555; the Kitt Peak National Observatory and the Cerro Tololo Inter-American Observatory operated by the Association of Universities for Research in Astronomy, Inc., under cooperative agreement with the National Science Foundation; and the San Pedro Mártir Observatory operated by the Universidad Nacional Autónoma de México. We have made extensive use of the SIMBAD database, operated at CDS, Strasbourg, France, and its mirror site at Harvard University and NASA's Astrophysics Data System Bibliographic Services. G.J.F. acknowledges support by NSF (1816537, 1910687), NASA (ATP 17-ATP17-0141), and STScI (HST-AR- 15018).

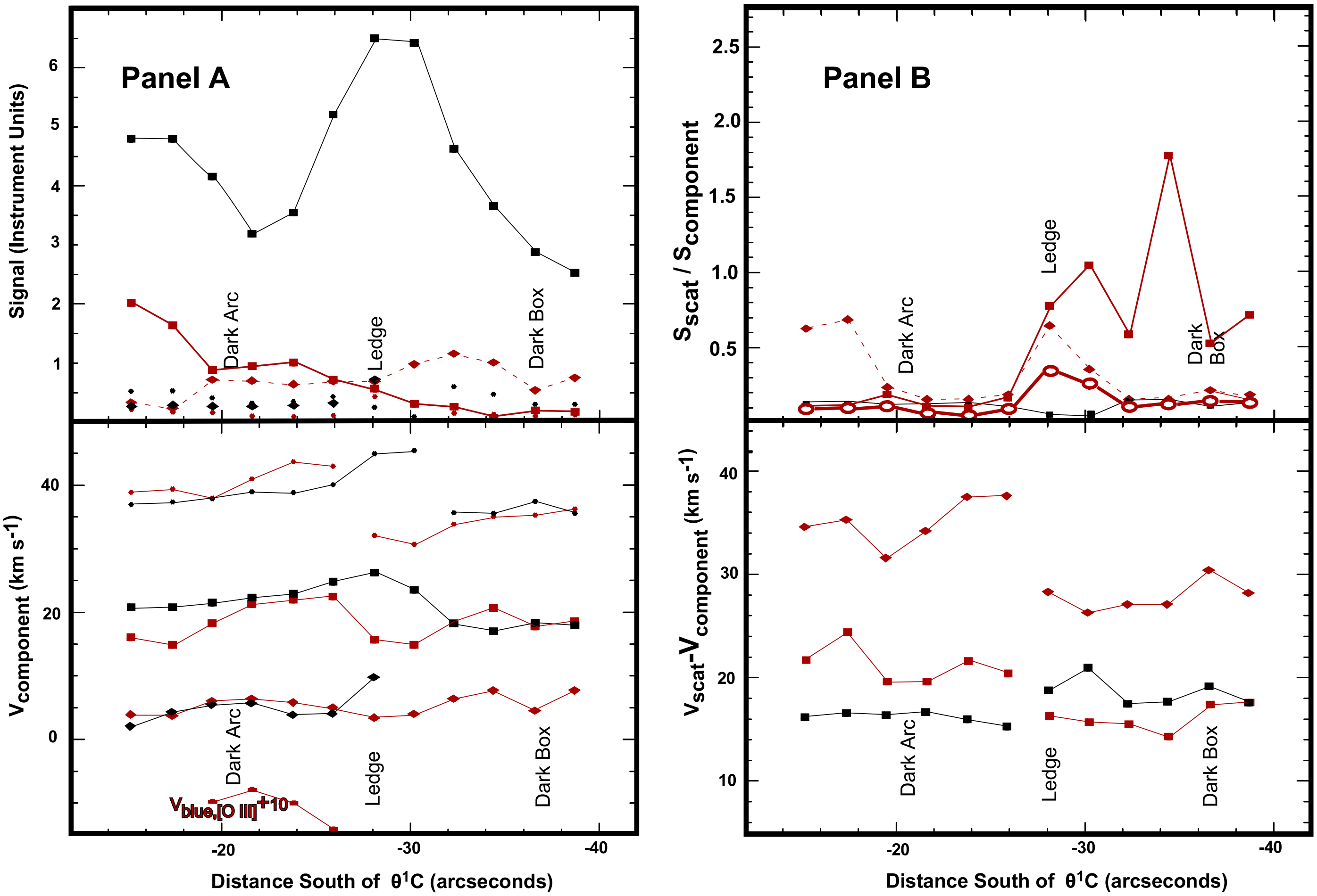

Figure 7. This figure is similar to Figure 5 except that it shows data from a profile at an R.A. displacement 38″ west of θ^1 Ori C passing through the center of the Ledge feature in the center of the Crossing. The symbols mean the same as in Figure 5, but the red ellipses indicate $S_{\mathrm{scat,[O\ III]}}/(S_{\mathrm{short,[O\ III]}}+S_{\mathrm{long,[O\ III]}})$. In panel (A), velocities and signals are shown. Weak but clear $V_{\mathrm{blue,[O\ III]}}$ components are also shown in their correct displacements but at velocities 10 km s^{-1} greater than measured. In panel (B), scattered-light ratios and velocity differences are shown.

Appendix
A Profile across the Ledge Feature at the Center of the Crossing

At the center of the 38″ west profile lies a narrow E–W feature within the larger feature previously called the West Jet. It does not have any measured radial and tangential velocities (O'Dell et al. 2015; Paper IV), thus arguing that the name originally assigned to it (the West Jet) is misleading. The small $V_{\mathrm{long,[N\ II]}}$ peak there and the large increase in $S_{\mathrm{long,[N\ II]}}$ mean that it is a small ionized region seen nearly edge on; therefore, a designation like the Ledge is more descriptive. The higher side of the Ledge lies to the south, otherwise, there would be a shadowed zone in that direction.

Figure 7 shows the results along the RA 38 profile. Proceeding south in the upper portion of panel (A), we see that there are dips in $S_{\mathrm{long,[N\ II]}}$ and $S_{\mathrm{long,[O\ III]}}$ along the Dark Arc, with the minimum of $S_{\mathrm{long,[O\ III]}}$ being slightly farther north, at which point $S_{\mathrm{short,[O\ III]}}$ begins to increase. The large rise in $S_{\mathrm{long,[N\ II]}}$ but the continuation of a decreasing trend in $S_{\mathrm{long,[O\ III]}}$ south of the Dark Arc is consistent with the much higher spatial resolution images in Figures 3 and 4. This indicates that the [O III]-emitting layer is thicker than the size of the Dark Arc in the plane of the sky. $S_{\mathrm{long,[O\ III]}}$ decreases south of the Ledge while $S_{\mathrm{short,[O\ III]}}$ remains strong, indicating that the $S_{\mathrm{short,[O\ III]}}$ component has become dominant.

In the lower portion of panel (A), one sees that the $V_{\mathrm{long,[N\ II]}}$ component slowly increases until the Ledge is reached. This can be interpreted as an increasing tilt of the ionized layer removing more of the photoevaporation flow velocity, and after the peak velocity at the Ledge, the drop in $V_{\mathrm{long,[N\ II]}}$ and $V_{\mathrm{long,[O\ III]}}$ indicate the south side of the Ledge is flatter than the north. The disappearance of the $V_{\mathrm{short,[N\ II]}}$ component south of the Ledge indicates that the gas that had been producing it is no longer there, probably by having become more ionized.

In the lower portion of panel (B), we see that $V_{\mathrm{scat,[N\ II]}} - V_{\mathrm{long,[N\ II]}}$ is about the same (16 ± 1 km s^{-1}) as found in Table 1 for the Crossing, and the slight shift to a larger value south of the Ledge is consistent with this region being flatter. In [O III], the velocity is again similar to the Crossing value in Table 1 (20 ± 3 km s^{-1}), but it is unclear why the difference decreases to the south, although this may be due to the $V_{\mathrm{long,[O\ III]}}$ feature becoming weak there. Similarly, the high values in $S_{\mathrm{scat,[O\ III]}}/S_{\mathrm{short,[O\ III]}}$ (upper portion of panel (B)) occur in the north, where $S_{\mathrm{short,[O\ III]}}$ is weak and becomes appropriately low in the south where $S_{\mathrm{short,[O\ III]}}$ is strong. This means that even in [O III], the $V_{\mathrm{scat,[O\ III]}}$ is backscattered light from the nearest strong emitting layer. This is illustrated by the series of data points giving the $S_{\mathrm{scat,[O\ III]}}/(S_{\mathrm{short,[O\ III]}}+S_{\mathrm{long,[O\ III]}})$ values. The local rise in the Ledge samples probably means that our simple backscattering model breaks down there.

In the upper panel of the upper portion of panel (B), we see that the ratio $S_{\text{scat,[N II]}}/S_{\text{long,[N II]}}$ is always small, as one would expect from $V_{\text{long,[N II]}}$ radiation being backscattered from a nearby PDR. Again, [O III] is more complex. However, in the north region, where $V_{\text{long,[O III]}}$ is strongest, the $S_{\text{scat,[O III]}}/S_{\text{long,[O III]}}$ values are small again, like backscattering. Then, the ratio becomes impossibly large to the south, indicating that it is not the source of $V_{\text{scat,[O III]}}$; but, this is the region where $V_{\text{long,[O III]}}$ has become weaker than $V_{\text{short,[O III]}}$.

In the lower portion of panel (A), we show the locations of four very blue (about $-20\ \text{km s}^{-1}$) and weak (about 1% of $S_{\text{long,[O III]}}$) [O III] velocity components.

The averaged results differ by no statistically significant amounts from the lower-resolution-profile results given under the Crossing heading in Table 1. There are two surprising results here: that the [N II]-strong Ledge shows no difference in its radial velocity from that of the surrounding nebula and that the dark features do not contain velocity differences.

ORCID iDs

C. R. O'Dell https://orcid.org/0000-0003-3323-2310
N. P. Abel https://orcid.org/0000-0003-1791-723X
G. J. Ferland https://orcid.org/0000-0003-4503-6333

References

Abel, N. P., Ferland, G. J., & O'Dell, C. R. 2019, ApJ, 881, 130
Abel, N. P., Ferland, G. J., O'Dell, C. R., & Troland, T. H. 2016, ApJ, 819, 136
Baldwin, J. A., Ferland, G. J., Martin, P. G., et al. 1991, ApJ, 374, 580
García-Díaz, M.-T., Henney, W. J., López, J. A., & Doi, T. 2008, RMxAA, 44, 181
Goicoechea, J. R., Pety, J., Quadrado, S., et al. 2016, Natur, 537, 207
Goicoechea, J. R., Teyssier, D., Etxaluze, M., et al. 2015, ApJ, 812, 75
Güdel, M., Briggs, K. R., Montmerle, T., et al. 2008, Sci, 319, 309
Henney, W. J. 1998, ApJ, 503, 760
Henney, W. J., Arthur, S. J., & García-Díaz, M.-T. 2005, ApJ, 627, 813
Johnston, K. J., Palmer, P., Wilson, T. L., & Bieging, J. H. 1983, ApJ, 271, 89
Kounkel, M., Hartmann, L., Loinard, L., et al. 2017, ApJ, 834, 142
Mangum, J. G., Wootten, A., & Plambeck, R. L. 1993, ApJ, 409, 282
Mesa-Delgado, A., Núñez-Díaz, M., Esteban, C., López-Martín, L., & García-Rojas, J. 2011, MNRAS, 417, 420
O'Dell, C. R. 2018, MNRAS, 478, 1017
O'Dell, C. R., Abel, N. P., & Ferland, G. J. 2020, ApJ, 891, 46
O'Dell, C. R., Abel, N. P., & Ferland, G. J. 2021, ApJ, 907, 119
O'Dell, C. R., Ferland, G. J., Henney, W. J., et al. 2015, AJ, 150, 108
O'Dell, C. R., Henney, W. J., Abel, N. P., et al. 2009, AJ, 137, 367
O'Dell, C. R., Muench, A., Smith, N., & Zapata, L. 2008, in Handbook of Star Forming Regions, Vol. 1: The Northern Sky, ed. B. Reipurth (San Fransisco, CA: ASP Monograph Publications), 544
O'Dell, C. R., & Wong, S. K. 1996, AJ, 111, 846
O'Dell, C. R., & Yusef-Zadeh, F. 2000, ApJ, 120, 382
Osterbrock, D. E., & Ferland, G. J. 2006, Astrophysics of Gaseous Nebulae and Active Galactic Nuclei (2nd ed.; Mill Valley, CA: Univ. Science Books)
Pabst, C., Goicoechea, J. R., Teyssier, D., et al. 2020, A&A, 639, 2
Pabst, C., Higgins, R., Goicoechea, J. R., et al. 2019, Natur, 565, 618
Peng, T.-C., Wyrowski, F., Zapata, L. A., Güsten, R., & Menten, K. M. 2012, A&A, 538, A12
Stacy, G. J., Jaffe, D. T., Geis, N., et al. 1993, ApJ, 404, 219
Tatematsu, K., Umemoto, T., Heyer, M. H., et al. 1998, ApJS, 118, 517
Tielens, A. G. G. M., Meixner, M. M., van der Werf, P. P., et al. 1993, Sci, 262, 86
Troland, T. H., Goss, W. M., Brogan, C. R. M., & Roberts, D. A. 2016, ApJ, 825, 2
van der Werf, P. P., & Goss, W. M. 1989, A&A, 224, 209
van der Werf, P. P., Goss, W. M., & O'Dell, C. R. 2013, ApJ, 762, 101